Fast Track

Benjamin G. Hawkins[1]
Brian J. Kirby[2]

[1]Department of Biomedical Engineering, College of Engineering, Cornell University, New York, USA
[2]Sibley School of Mechanical and Aerospace Engineering, College of Engineering, Cornell University, New York, USA

Research Article

Electrothermal flow effects in insulating (electrodeless) dielectrophoresis systems

We simulate electrothermally induced flow in polymeric, insulator-based dielectrophoresis (iDEP) systems with DC-offset, AC electric fields at finite thermal Péclet number, and we identify key regimes where electrothermal (ET) effects enhance particle deflection and trapping. We study a single, two-dimensional constriction in channel depth with parametric variations in electric field, channel geometry, fluid conductivity, particle electrophoretic (EP) mobility, and channel electroosmotic (EO) mobility. We report the effects of increasing particle EP mobility, channel EO mobility, and AC and DC field magnitudes on the mean constriction temperature and particle behavior. Specifically, we quantify particle deflection and trapping, referring to the deviation of particles from their pathlines due to dielectrophoresis as they pass a const riction and the stagnation of particles due to negative dielectrophoresis near a constriction, respectively. This work includes the coupling between fluid, heat, and electromagnetic phenomena *via* temperature-dependent physical parameters. Results indicate that the temperature distribution depends strongly on the fluid conductivity and electric field magnitude, and particle deflection and trapping depend strongly on the channel geometry. Electrothermal (ET) effects perturb the EO flow field, creating vorticity near the channel constriction and enhancing the deflection and trapping effects. ET effects alter particle deflection and trapping responses in insulator-based dielectrophoresis devices, especially at intermediate device aspect ratios ($2 \leq r \leq 7$) in solutions of higher conductivity ($\sigma_m \geq 1 \times 10^{-3}$ S/m). The impact of ET effects on particle deflection and trapping are diminished when particle EP mobility or channel EO mobility is high. In almost all cases, ET effects enhance negative dielectrophoretic particle deflection and trapping phenomena.

1 Introduction

Dielectrophoresis (DEP) is the transport of polarizable particles in response to a non-uniform electric field, exclusive of electrophoresis [1]. DEP forces depend on the

Correspondence: Dr. Brian J. Kirby, 238 Upson Hall, Cornell University, Ithaca, NY, 14853, USA
E-mail: bk88@cornell.edu
Fax: +1-6072551222

Abbreviations: DEP, dielectrophoresis; **eDEP,** electrode-based dielectrophoresis; **EO,** electroosmosis; **EP,** electrophoresis; **ET,** electrothermal; **iDEP,** insulator-based dielectrophoresis

magnitude and non-uniformity of the electric field, as well as the complex permittivity of a particle and its surrounding media [2]. The complex permittivities ($\tilde{\varepsilon} = \varepsilon - i\sigma/\omega$) of the particle and surrounding media are a function of the frequency of the polarizing electric field; the permittivity, ε, is assumed independent of frequency in most DEP experiments [3]. The combination of material and frequency dependence makes DEP a useful technique for researchers attempting to manipulate, separate, and characterize particles and cells. DEP devices have been used to characterize and separate a variety of species [4], *e.g.* bacterial populations [5–8], mammalian cells [9–12], DNA [13], proteins [14–17], and viruses [18].

Electric field non-uniformities in DEP devices are most often generated *via* microfabricated electrodes (electrode-based DEP, eDEP) or insulating constrictions in channel cross-sectional area (insulator-based DEP, iDEP). eDEP devices rely on microfabricated electrodes embedded within the fluid channel. iDEP devices rely on macroscopic electrodes placed in external reservoirs, making device fabrication less time consuming and less expensive. They can be fabricated *via* hot embossing in low-cost polymeric substrates in a matter of hours (after making a silicon master) [19]; even glass iDEP devices, which require longer fabrication processes, are of relatively low cost because they do not require internal, microfabricated electrodes. iDEP devices can be made from a variety of materials – from glass and silicon to polymers such as Zeonor and polycarbonate. Compared with eDEP devices, iDEP devices require relatively large electric potentials to generate equivalent electric fields, limiting the range of field frequencies owing to the slew-rate limitations of high-voltage equipment. Recent work has shown that DC-offset, AC electric fields (of low-frequency) can enhance the operation of iDEP devices by decoupling EO and electrophoretic (EP) effects from DEP [19, 20]. We have previously demonstrated continuous-flow iDEP separation of polystyrene microspheres in Zeonor devices using DC-offset, AC electric fields [19]. As researchers continue to apply iDEP techniques to cellular analysis, it becomes increasingly relevant to investigate the potentially confounding effects of Joule heating and electrothermal (ET) flow.

DEP, either in electrode-based or insulating devices, is achieved by subjecting samples to a non-uniform electric field. Therefore, localized Joule heating is ever-present and particularly significant in high-conductivity solutions actuated by high electric fields, as is often desirable in cellular experiments in DEP devices. In addition to the temperature-specific implications for cellular response and viability, localized Joule heating creates gradients in temperature-dependent media properties, leading to electrothermally induced fluid motion [21]. Although some researchers have used Joule heating to facilitate PCR and chemical reactions, or leveraged ET flows to enhance particle trapping [22, 23] and pump fluids [24, 25], most avoid these effects by using low-conductivity solutions to minimize Joule heating.

In eDEP systems, ET forces manifest as localized regions of recirculation. Locally recirculating regions have been observed *via* analyte or tracer particles [23, 26–30] and predicted *via* numerical simulation [24, 30–35]. Experimental observations of recirculatory motion exhibited by trapped particles in iDEP devices have been anecdotally attributed to ET effects, but no effort to date has modeled or experimentally confirmed this explanation. The majority of experimental and numerical works in eDEP devices do not consider the fully coupled thermal-fluid-electrical problem, electing instead to solve the systems sequentially, solving for the electric field, then the resulting temperature field, and finally the induced ET flow field. In many cases, the independent solutions approach is appropriate, owing to the low

thermal Péclet number, Pe_T. In iDEP systems, however, Pe_T is not small and thus we consider the fully coupled problem.

Because ET flow can affect the use of iDEP devices for particle and cellular analysis, we present a numerical investigation of ET flow in iDEP systems with the goals of determining the magnitude of ET forces and examining their impact on particle deflection and trapping. Deflection (the deviation of particles from their pathlines due to DEP as they pass a constriction) and trapping (the stagnation of particles due to negative DEP near a constriction) are the two modes of negative DEP actuation common in iDEP systems. In modeling ET flow at finite Pe_T, we simulate the coupling of thermal, electrical, and fluid mechanical systems. As a basis for our analysis, we choose a constriction in channel depth because it is commonly used (Fig. 1) for particle manipulation [36–41].

2 Theory

In this section, we present three sets of coupled equations representing the physics of fluid, electrical, and thermal formulae as applied to the commonly used insulating constriction geometry [36–38, 40]. We present first the physical equations, then discuss appropriate approximations, and finally present the specific expressions used for numerical simulations in this work. We will re-express the general governing equations in terms of a DC-offset, AC electric field, which is relevant to our previous work [19]. The insulating constriction is considered in two dimensions with variation in the constriction height.

Temperature is the primary coupling variable between electrical, fluid, and thermal governing equations: heat is generated as a result of the applied electric field by Joule heating; this heat is conducted through the channel walls or convected by pressure-driven flow, EO flow, electrothermally induced flow, or combinations thereof. We consider the following temperature-dependent material properties: electrical conductivity (σ_m), electrical permittivity (ε_m), thermal conductivity (k_m), specific heat (C_p), and viscosity (η). Local variations in these material properties influence the resulting fluid, thermal, and electrical physics: (i) the ET body force and EO flow velocity depend on σ_m and ε_m, (ii) the heat flux depends on k_m and C_p, and (iii) the electric field and Joule heating depend on σ_m and ε_m. This coupling forms a non-linear relationship between the three sets of governing equations (fluid, electrical, and thermal).

2.1 Electromagnetics

The governing equations for electrokinetic and ET phenomena discussed here are the quasi-static Maxwell's equations for inhomogeneous materials. We consider sinusoidal electric fields of single and multiple frequencies. For simplicity, we express sinusoidal quantities, such as the electric field, in complex notation when we are deriving
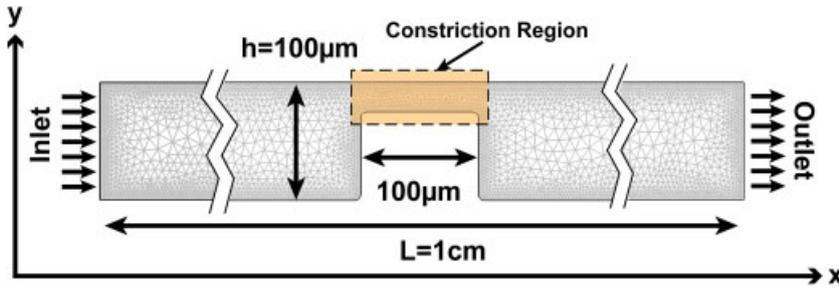
Figure 1. Insulating constriction geometry showing inlet, outlet, flow direction, and constriction region. Mesh shown is used in numerical simulations on the fluid domain. Axes are used as reference directions throughout this work.

frequency-dependent expressions. Generally,

$$\mathbf{E}(t, \omega) = \Re[\tilde{E} \exp(i\omega t)]$$

$$\mathbf{E}(t, \omega_0, \omega_1, \ldots, \omega_n) = \Re\left[\sum_n \tilde{E}_n \exp(i\omega_n t)\right], \tag{1}$$

where $\Re[\cdots]$ isolates the real component of $[\cdots]$, $\tilde{E} = E \exp(i\vartheta)$ is the electric field phasor containing spatially dependent phase information, and the tilde ($\tilde{f}$) denotes a complex quantity. In this work, the electric field phase is uniform and so $\vartheta = 0$ and $\tilde{E}$ is purely real. We will use these complex expressions to present general analytical results and use their time-averaged real component for numerical computation.

In the absence of accelerating charge (this quasi-static assumption is valid where the wavelength of the electromagnetic field is large compared with the size of the system [42], and implies $\nabla \times \mathbf{E} = -\partial B/\partial t = 0$), Gauss's law (Eq. 2) and charge conservation (Eq. 3) are written as

$$\nabla \cdot (\varepsilon_m \mathbf{E}) = \rho_e \tag{2}$$

$$\nabla \cdot (\sigma_m \mathbf{E} + \rho_e \mathbf{u}) + \frac{\partial \rho_e}{\partial t} = 0 \tag{3}$$

where bolded variables denote vector fields, ρ_e is the volumetric charge density, and the $\rho_e \mathbf{u}$ term represents the convective charge flux density. We neglect charge transport due to diffusion because it is dominated by charge transport due to electrophoresis. Following Ramos *et al.* [43] we additionally assume that ohmic current ($\sigma_m \mathbf{E}$) rearranges charge faster than fluid flow ($\rho_e \mathbf{u}$). Therefore, in the remainder of this work, we neglect the convection of charge due to fluid motion.

2.2 Hydrodynamics

We describe the time-averaged hydrodynamics of EO and ET fluid flow using the time-averaged Navier–Stokes equations with appropriate boundary conditions. For incompressible fluids [44]:

$$\rho_m \left(\frac{\partial \mathbf{u}}{\partial t} + \mathbf{u} \cdot \nabla \mathbf{u} \right) = -\nabla p + \nabla \cdot (\eta \nabla \mathbf{u}) + \mathbf{f} \tag{4}$$

where ρ_m is mass density, η is the dynamic viscosity, p is time-averaged pressure, $\mathbf{u}$ is the time-averaged fluid velocity, and $\mathbf{f}$ is a volumetric body force. In this work, we consider only flows where the fluid velocity is constant when averaged over the period of the electric field ($\partial \mathbf{u}/\partial t = 0$).

2.2.1 EO flow

Electroosmosis is often used to drive fluid motion in microfluidic systems and arises owing to the EP motion of mobile counterions accumulated in the double layer near the channel wall. For system sizes that are large (10–100 μm) compared with the double layer ($\lambda_D \sim 10$ nm), fluid motion outside the double layer can be approximated *via* a slip boundary condition on the bulk fluid according to the Smoluchowski equation [45]

$$\mathbf{u}_{EO} = -\frac{\varepsilon_m \zeta_w}{\eta} \mathbf{E} \tag{5}$$

$$\mu_{EO} = -\frac{\varepsilon_m \zeta_w}{\eta} \tag{6}$$

at the interface. We define an EO mobility, μ_{EO}, and a phenomenological potential, ζ_w, that defines the no-slip boundary condition applied within the electrical double layer [46, 47]. We assume that the thickness of the double layer does not change significantly – relative to the size of the channel – as a function of temperature and for simplicity treat ζ_w as independent of temperature.

2.2.2 Electrothermal flow

ET flow arises in systems with non-uniform permittivity and conductivity. In such a system, a local free charge distribution must be present if Gauss's Law (Eq. 2) and charge conservation are to be satisfied simultaneously. Local charge density, both free and bound, responds to the applied electric field, resulting in a non-zero body force on the fluid:

$$\mathbf{f}_{ET} = \rho_e \mathbf{E} - \frac{1}{2} |\mathbf{E}|^2 \nabla \varepsilon_m \tag{7}$$

The first and second terms on the right-hand side express the Coulomb force on free and bound charges, respectively. Following the analysis of Ramos *et al.* [43], we perform a perturbative expansion of the electric field around this isothermal solution. We assume that changes in ε_m and σ_m are small and consider a small perturbation, $\mathbf{E}_1$, to the electric field, $\mathbf{E}_0$, that would be present in the isothermal case: $\mathbf{E} = \mathbf{E}_0 + \mathbf{E}_1$ where $|\mathbf{E}_1| \ll |\mathbf{E}_0|$. The isothermal solution is assumed to be electroneutral ($\nabla \cdot \mathbf{E}_0 = 0$), therefore small perturbations in the charge density are associated only with $\mathbf{E}_1$. As a result, we write the charge density (from Gauss's Law, Eq. 2) as:

$$\rho_e = \nabla \varepsilon_m \cdot \mathbf{E}_0 + \varepsilon_m \nabla \cdot \mathbf{E}_1 \tag{8}$$

The continuity equation (3) can be expanded as:

$$\nabla \sigma_m \cdot \mathbf{E}_0 + \sigma_m \nabla \cdot \mathbf{E}_1 + \frac{\partial}{\partial t}(\nabla \varepsilon_m \cdot \mathbf{E}_0 + \varepsilon_m \nabla \cdot \mathbf{E}_1) = 0 \qquad (9)$$

We further expand this representation to include an electric field with multiple sinusoidal components, take the Fourier transform with respect to time ($F[\mathbf{E}] = \underline{\mathbf{E}}$), and solve for $\nabla \cdot \underline{\mathbf{E}}_1$:

$$0 = \nabla \sigma_m \cdot \underline{\mathbf{E}}_0 + \sigma_m \nabla \cdot \underline{\mathbf{E}}_1 + i\omega(\nabla \varepsilon_m \cdot \underline{\mathbf{E}}_0 + \varepsilon_m \nabla \cdot \underline{\mathbf{E}}_1)$$

$$\nabla \cdot \underline{\mathbf{E}}_1 = \frac{-(\nabla \sigma_m + i\omega \nabla \varepsilon_m) \cdot \underline{\mathbf{E}}_0}{\sigma_m + i\omega \varepsilon_m} \qquad (10)$$

from this we can write the Fourier transform of the charge density as:

$$\underline{\rho}_e = \frac{(\sigma_m \nabla \varepsilon_m - \varepsilon_m \nabla \sigma_m) \cdot \underline{\mathbf{E}}_0}{\sigma_m + i\omega \varepsilon_m} \qquad (11)$$

Note that ω is the independent variable in frequency space and not equivalent to ω_n in Eq. (1). Returning to the time domain by applying the inverse Fourier transform ($F^{-1}[\underline{\rho}_e] = \rho_e$), we can re-write Eq. (7) explicitly:

$$\mathbf{f}_{ET} = \sum_n \left(\frac{\sigma_m \nabla \varepsilon_m - \varepsilon_m \nabla \sigma_m}{\sigma_m + i\omega_n \varepsilon_m} \cdot \tilde{\mathbf{E}}_n \exp(i\omega_n t) \right) \sum_k \tilde{\mathbf{E}}_k \exp(i\omega_k t)$$

$$- \frac{1}{2} \sum_n \tilde{\mathbf{E}}_n \exp(i\omega_n t) \sum_k \tilde{\mathbf{E}}_k \exp(i\omega_k t) \nabla \varepsilon_m \qquad (12)$$

Taking the time average and invoking orthogonality (only terms where $n = k$ are non-zero when averaged over time), we find:

$$\langle \mathbf{f}_{ET} \rangle = \frac{1}{2} \Re \left[\sum_n \left(\frac{\sigma_m \nabla \varepsilon_m - \varepsilon_m \nabla \sigma_m}{\sigma_m + i\omega_n \varepsilon_m} \cdot \tilde{\mathbf{E}}_n \right) \tilde{\mathbf{E}}_n \right]$$

$$- \frac{1}{4} \Re[\tilde{\mathbf{E}}_n \cdot \tilde{\mathbf{E}}_n] \nabla \varepsilon_m \qquad (13)$$

Eq. (13) shows that the real, time-average ET force obeys superposition.

2.3 Thermodynamics

In this section, we examine several thermodynamic contributions: (i) the conduction of heat through the fluid and channel boundaries, (ii) the convection of heat through the channel, and (iii) the effect of temperature-dependent solid, fluid, and electrical material properties.

2.3.1 Temperature-dependent parameters

In this work, we consider temperature-dependent viscosity (η), thermal conductivity (k_m), specific heat (C_p), electrical conductivity (σ_m), and permittivity (ε_m). The ionic solutions considered in this work are of low concentration such that mechanical parameters (η, k_m, and C_p) are approximately independent of concentration. Electrical conductivity of electrolytes increases 2.2%/K [48]. Viscosity, thermal

conductivity, specific heat, and electrical permittivity are modeled using polynomial fits of data taken from [49] between 273 and 373 K with coefficient values listed in Table 1:

$$\eta = a_0 + a_1 T + a_2 T^2 + a_3 T^3 + a_4 T^4 + a_5 T^5 + a_6 T^6 \qquad (14)$$

$$k_m = b_0 + b_1 T + b_2 T^2 + b_3 T^3 \qquad (15)$$

$$C_p = c_0 + c_1 T + c_2 T^2 + c_3 T^3 + c_4 T^4 \qquad (16)$$

$$\varepsilon_m = d_0 + d_1 T + d_2 T^2 \qquad (17)$$

2.3.2 Joule heating

Localized Joule heating near a channel constriction is a source of temperature gradients that lead to spatial variations in material properties and associated ET flow phenomena. Joule heating corresponds to the electrical energy generated *per* unit volume

$$q = \mathbf{J} \cdot \mathbf{E} = \sigma_m \mathbf{E} \cdot \mathbf{E} \qquad (18)$$

where $\mathbf{J}$ is the electric current. The energy generated by Joule heating depends on the temperature distribution *via* σ_m.

2.3.3 Heat conduction and convection

Heat is transferred through the system by convection and conduction. Heat generated by Joule heating is dissipated through the fluid and substrate by conduction and transported downstream by convection according to Eq. (19) [50]

$$\rho_m C_p \frac{\partial T}{\partial t} + \rho_m C_p \mathbf{u} \cdot \nabla T = k_m \nabla^2 T + \sigma_m \mathbf{E} \cdot \mathbf{E} \qquad (19)$$

where we have neglected viscous dissipation; the temperature (T) and electric field are time-averaged. The thermal Péclet number, which compares magnitude of heat convection with

Table 1. Coefficient values used to model the temperature dependence of the fluid media's viscosity, η (a_n coefficients, Eq. 14), thermal conductivity, k_m (b_n coefficients, Eq. 15), specific heat at constant pressure, C_p (c_n coefficients, Eq. 16), and electrical permittivity, ε_m (d_n coefficients, Eq. 17).

Coefficient	Value	Coefficient	Value
a_0	1.379957	c_0	1.201×10^4
a_1	-2.112402×10^{-2}	c_1	-80.407
a_2	1.360456×10^{-4}	c_2	0.30987
a_3	-4.64509×10^{-7}	c_3	-5.3819×10^{-4}
a_4	8.904274×10^{-10}	c_4	3.6254×10^{-7}
a_5	$-9.079069 \times 10^{-13}$		
a_6	3.845733×10^{-16}		
b_0	-8.69×10^{-1}	d_0	251.1
b_1	8.948×10^{-3}	d_1	-0.7992
b_2	-1.5836×10^{-5}	d_2	7.375×10^{-4}
b_3	7.9754×10^{-9}		

heat diffusion

$$\frac{|\rho_m C_p \mathbf{u} \cdot \nabla T|}{|k_m \nabla^2 T|} \approx \frac{\rho_m C_p |\mathbf{u}| l}{k_m} \equiv Pe_T \tag{20}$$

is of order 1 in this work owing to the thermally insulating nature of the surrounding plastic substrate, large fluid speeds, and large temperature gradients in the constriction region. Therefore, in this work, we choose to retain the convective term. We examine only stationary, time-averaged solutions, so we neglect the first term on the left-hand side of Eq. (19), resulting in

$$\rho_m C_p \mathbf{u} \cdot \nabla T = k_m \nabla^2 T + \sigma_m \mathbf{E} \cdot \mathbf{E} \tag{21}$$

In addition to heat conduction and convection within the fluid domain, we model conductive heat transfer through the channel walls and into the air surrounding the device. To do this, we consider a 100-μm-deep channel embedded between two 1-mm-thick Zeonor (plastic) substrates. This defines five regions in a two-dimensional model: air (above and below), Zeonor substrate (above and below), and the channel. There are four distinct interfaces to consider, of two types: air/Zeonor and Zeonor/water. These four interfaces correspond to a device placed on an inverted microscope stage, where free convection occurs on top and bottom of the device. We treat the air/Zeonor interfaces by extracting a heat transfer coefficient from empirically determined Rayleigh (Re_ℓ) and average Nusselt ($\overline{Nu}_\ell$) numbers [50].

$$\overline{Nu}_\ell = 0.54\, Ra_\ell^{1/4} \tag{22}$$
$$= \frac{h_{a/Z}\ell}{k_a}$$
$$\approx \frac{1}{2} \sqrt[4]{\frac{g\beta_a a \ell^3}{\alpha_a \nu_a} (T_{a,Z} - T_0)} \tag{23}$$

where ℓ is the ratio of device area to perimeter, $k_a = 0.028$ W/m K is the thermal conductivity of air, $h_{rma/Z}$ is the heat transfer coefficient for the air/Zeonor interface, T_0 is the room or reservoir temperature (far from the interface), and $g\beta_a/\alpha_a\nu_a$ is a ratio of thermal convection and conduction constants. g is acceleration due to gravity, β_a is the thermal expansion coefficient of air, α_a is the thermal diffusivity of air, and ν_a is the kinematic viscosity of air. The lower interface is characterized by a slightly different relationship [50]:

$$\overline{Nu}_\ell \approx \frac{1}{4} Ra_\ell^{1/4} \tag{24}$$

For purposes of estimation, we assume that the heat transfer occurs in one dimension, and we balance the heat flux across both air/Zeonor and Zeonor/water interfaces

$$q_{a,Z} = h_{a,Z}(T_{a,Z} - T_0) \tag{25}$$
$$= \frac{k_Z}{\ell}(T_{Z,w} - T_{a,Z}) = q_{Z,w} \tag{26}$$

where $T_{a,Z}$ and $T_{Z,w}$ are the temperatures at the air/Zeonor and Zeonor/water interfaces, respectively, and $k_Z = 0.147$ W/m K is the thermal conductivity of Zeonor [51]. Solving for the

linearized heat transfer coefficient across the air/Zenor interface, we obtain:

$$\text{Upper}: h_{a,Z} \approx \frac{k_a l}{2k_Z \ell} \sqrt[4]{\frac{g\beta_a \ell^3}{\alpha_a \nu_a}(T_{a,Z} - T_0)} \tag{27}$$

$$\text{Lower}: h_{a,Z} \approx \frac{k_a l}{4k_Z \ell} \sqrt[4]{\frac{g\beta_a \ell^3}{\alpha_a \nu_a}(T_{a,Z} - T_0)} \tag{28}$$

These expressions give boundary conditions for the upper and lower air/Zeonor interfaces. In addition, to eliminate the substrate material from the computational domain and reduce computation time, we define a linearized thermal conductivity term that is determined by fitting

$$(T_{Z,w} - T_{a,Z})^4 = \frac{g\beta_a \ell^3}{32\alpha_a \nu_a}\left(\frac{lk_a}{\ell k_Z}\right)^4 (T_{a,Z} - T_0) \tag{29}$$

where $l = 1$ mm is the thickness of the Zeonor substrate and is a result of linearizing heat transfer through the substrate. Plotting $T_{a,Z}$ *versus* $T_{Z,w}$ and fitting to a linear function at the top and bottom interfaces and averaging the results we obtain

$$\overline{q_{Z,w}} = \frac{k_Z}{l}\xi(T_{Z,w} - T_0) \tag{30}$$

where $\xi = 0.1286$ with $R^2 = 0.9$. Using Eqs. (27) and (28), we simulate the channel and the Zeonor substrate to assess the error introduced by our linearization and averaging. In these simulations, the applied voltage was swept from 1–250 V in a quiescent fluid. Results (not shown) show less than 2% error.

2.4 Particle electrokinetics

2.4.1 Electrophoresis

Electrophoresis drives particle motion in the direction of the local electric field. For particles whose radius is significantly greater than the thickness of their double layer ($\lambda_D << a$), particle EP velocity can be described by a Smoluchowski equation

$$\mathbf{u}_{EP} = \frac{\varepsilon_m \zeta_p}{\eta}\mathbf{E} \tag{31}$$

where ζ_p is a phenomenological potential that defines the no-slip boundary condition within the particle double layer.

2.4.2 Dielectrophoresis

DEP results from the Coulomb force on bound charge at the interface between fluid and particle (resulting from a discontinuity in complex permittivity). Given a homogeneous, isotropic, spherical particle in a homogeneous, infinite medium, the time-averaged DEP force can be written as [2]

$$\langle \mathbf{f}_{DEP} \rangle = \pi a^3 \varepsilon_m \Re[\tilde{f}_{CM}]\nabla(\mathbf{E} \cdot \mathbf{E}) \tag{32}$$

$$\tilde{f}_{CM} = \frac{\tilde{\varepsilon}_p - \tilde{\varepsilon}_m}{\tilde{\varepsilon}_p + 2\tilde{\varepsilon}_m} \tag{33}$$

where $\tilde{\epsilon} = \epsilon - i\sigma/\omega$ and $\tilde{f}_{CM}$ is the complex Clausius–Mossotti factor and contains the frequency dependence of the DEP force. In the limit as $\omega \to 0$, $\tilde{f}_{CM}$ can be expressed using purely real, conductive components of $\tilde{\epsilon}$. It has been shown that the DEP force obeys superposition for electric fields with multiple frequencies [19, 52]:

$$\langle \mathbf{f}_{DEP} \rangle = \pi a^3 \epsilon_m \sum_n \Re[\tilde{f}_{CM,n}] \nabla (\mathbf{E}_n \cdot \mathbf{E}_n) \tag{34}$$

where $\tilde{f}_{CM,n}$ is the complex Clausius–Mossotti factor at frequency ω_n.

3 Results and discussion

We conducted several sets of simulations with variations from a baseline case. The datum case parameters are listed in Table 2. We investigate how changes in channel geometry (r), fluid conductivity (σ_m), particle zeta potential (ζ_p), channel wall zeta potential (ζ_w), and the DC electric potential magnitude (V_{DC}), affect particle transport. Values are listed in Table 3. The channel geometry parameter, r, is the constriction ratio, defined as the bulk channel depth divided by the constriction depth (*e.g.* a 100 μm-wide channel that is constricted to 25 μm-wide would have a constriction ratio $r = 4$). For all cases, the AC-to-DC ratio, α, was varied from 0 to 50. Each case was also investigated with and without the ET body force term (Eq. 13).

3.1 Electrothermal flow

The ET body force acts opposite the direction of flow on the upstream side of the constriction, decreasing – and eventually reversing – fluid velocity as the force magnitude increases. The body force depends on gradients in fluid conductivity and permittivity. These gradients are temperature driven in this system and so the ET body force is directed down gradients in fluid temperature. In the iDEP constriction geometry, the temperature is highest in the constriction region and lowest at the channel entrance and the resulting ET body force is therefore directed away from the constriction, as shown in Supporting Information Fig. S1.

As α increases, the magnitude of the ET body force increases and perturbs the EO flow field. Figures 3A and B show how the flow field changes as α (and the ET body force) increases at two different locations near the constriction region: $x = 4.75$ mm and $x = 4.9$ mm. These figures highlight three key phenomena: (i) as α increases the fluid velocity in the center of the channel ($y = 50$ μm) decreases and reverses direction for $\alpha \geq 35$, (ii) as α increases

Table 2. Datum case for numerical simulations of ET flow.

σ_m (S/m)	$-\zeta_w$ (mV)	$-\zeta_p$ (mV)	r	V_{DC} (V)
0.01	40	60	4	10

Table 3. Simulation parameter sets for numerical simulations of ET flow. Each set isolates a particular variable from the datum state.

Simulation set	Variable (units)	Values
S1	r (unitless)	1.3, 1.7, 2.9, 3.3, 4, 5, 6.7, 10, 20
S2	σ_m (S/m)	5×10^{-2}, 1×10^{-2}, 5×10^{-3}, 1×10^{-3}, 5×10^{-4}, 1×10^{-4}, 5×10^{-5}, 1×10^{-5}, 5×10^{-6}, 1×10^{-6}
S3	$-\zeta_w$ (mV)	1, 5, 10, 20, 30, 40, 50, 60, 70, 80, 90, 100
S4	$-\zeta_p$ (mV)	0.01, 0.1, 1, 10, 20, 30, 40, 50, 60, 70, 80, 90, 100
S5	V_{DC} (V)	1, 5, 10, 15, 25, 50, 75, 100

the fluid velocity near the channel wall increases because the EO mobility increases as a function of temperature (η decreases more rapidly than ϵ_m in Eq. 6), and (iii) the fluid velocity distribution becomes skewed near the constriction because of locally fast electroosmosis in the constriction region, driven by higher electric fields and higher EO mobility (μ_{EO}).

3.2 Temperature

Channel temperature is of critical importance for experiments involving cellular samples. We choose to analyze the mean temperature in the constriction region, $\bar{T}_c$, because it represents the highest temperature region within the channel and it is the most sensitive to ET effects. The results of simulations with varying constriction ratio (r), solution conductivity (σ_m), wall zeta potential (ζ_w), and DC-field magnitude (V_{DC}) are reported in Fig. 4. Also reported is the percent difference in $\bar{T}_c$ due to ET flow.

The mean constriction temperature decreases with increasing constriction ratio and wall zeta potential. This is indicative of increased heat convection out of the constriction region. As the constriction ratio increases, the electric field within the constriction region increases and the EO flow velocity increases. This increase in heat convection competes with additional Joule heating in the constriction region, leading to a weak decrease in $\bar{T}_c$ as a function of constriction ratio. Similarly, changes in ζ_w change the EO flow velocity. In both cases, changing r or ζ_w, convection transports heat generated within the constriction region downstream, into the bulk of the channel. The result of increased convection due to increasing r or ζ_w is a decrease in $\bar{T}_c$. The influence of ET flow decreases with increasing r. The increased EO fluid velocity within the constriction region dominates the contributions from the ET body force, which acts opposite the direction of electroosmosis on the leading side of the constriction. The effects of ET flow on $\bar{T}_c$ were found to be independent of ζ_w over the range of test values.

$\bar{T}_c$ increases with increasing solution conductivity, σ_m, and DC field magnitude, V_{DC}. These results are indicative of
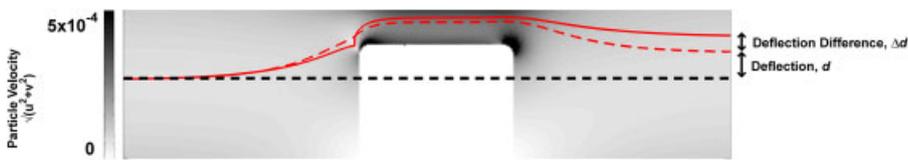
Figure 2. Particle deflection, *d*, and deflection difference, Δ*d*, are two metrics used to quantify ET effects in this work. Particle pathlines (red, color online) include the effects of electrophoresis, DEP, and fluid flow on particle motion with (solid) and without (dashed) an ET body force term in the Navier–Stokes equations. The background color table corresponds to particle velocity magnitude (|u|) in the baseline case, without ET flow. Simulation parameters are those listed in Table 2 with α = 38.
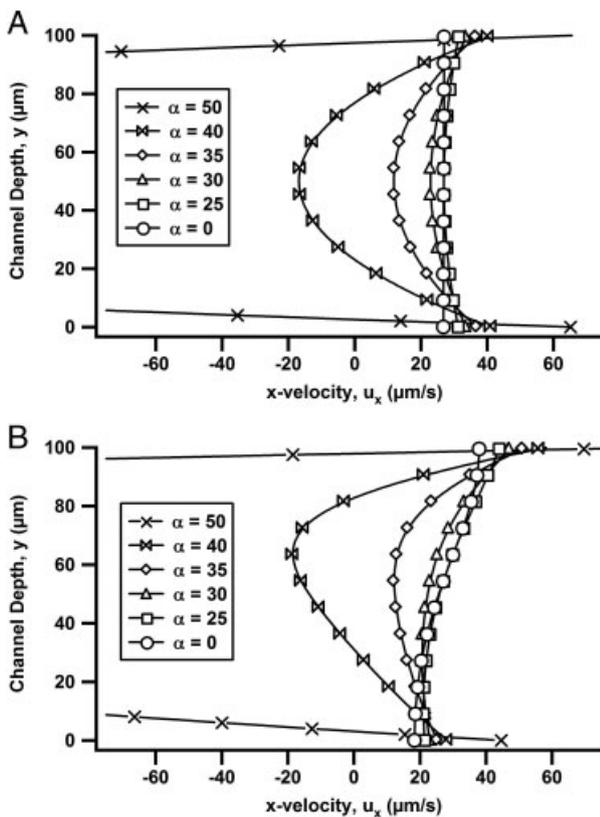

Figure 3. Profiles of fluid velocity in the *x*-direction plotted against channel height (*y*, Fig. 1) at select values of α. Velocity profiles are calculated at *x* = 4.75 mm in (A) and *x* = 4.9 mm in (B). The location *x* = 4.75 mm is upstream of the constriction by 200 μm where the flow is minimally perturbed by channel geometry, but the effects of ET flow are still prevalent. The location *x* = 4.9 mm is upstream of the constriction by 50 μm where the flow is perturbed by both channel geometry and ET flow. The upper portion of the fluid velocity profile is skewed closer to the constriction as a result of the increase in the EO flow velocity. Simulation parameters are listed in Table 2.

increased Joule heating (Eq. 18) in the constriction region. ET effects on $\bar{T}_c$ also increase with increasing σ_m and V_{DC}, owing to increased localized heat generation within the constriction region, which drives gradients in fluid conductivity and permittivity.

3.3 Particle deflection and trapping

Particle deflection and trapping are the two primary modes of operation for 2D and 3D iDEP techniques, respectively [19, 20, 37–39, 53, 54]. ET effects, in certain regimes, significantly enhance these phenomena by decreasing the local fluid velocity and increasing particle residence time. The particle deflection and trapping results for simulations with varying constriction ratio (*r*), solution conductivity (σ_m), particle zeta potential (ζ_p), channel wall zeta potential (ζ_w), and DC electric field magnitude (V_{DC}) are shown in Fig. 5. These results quantify particle deflection as a function of these parameters with varying AC-to-DC ratio, α, in the presence of ET flow, the percent difference between simulation results with and without the ET body force term in Equation 4, and the threshold value of α for particle trapping, $\alpha_{trapping}$.

Particle deflection is a strong function of constriction ratio and can be affected by ET flow. As the constriction ratio increases, the depth in the constriction region decreases and the electric field increases in order to satisfy conservation of current. This results in increasing electric field gradients and DEP forces. A particle approaching the constriction will be increasingly forced away from the constriction corners by nDEP as the constriction ratio increases (Fig. 5A). The effects of ET flow decrease with increasing constriction ratio and become significant only at higher values of α (Fig. 5B). As discussed above in Section 3.2 in the context of the mean constriction temperature, $\bar{T}_c$, the magnitude of the EO boundary condition within the constriction region increases with the constriction ratio and dominates the ET body force on the fluid as a result. This can be seen in Figs. 6A and B, in which recirculating flow is suppressed as the constriction ratio increases. Consistent with the results for particle deflection, the value of $\alpha_{trapping}$ is a strong function of the constriction ratio and is affected by ET flow at low constriction ratios, *r* < 6 (Fig. 5C). Beyond *r* = 6, the flow velocity within the constriction region obscures the effects of the ET body force.

Solution conductivity, σ_m, has a significant impact on $\bar{T}_c$, but does not significantly impact particle deflection (Fig. 5D). Rather, σ_m influences the magnitude of ET flow
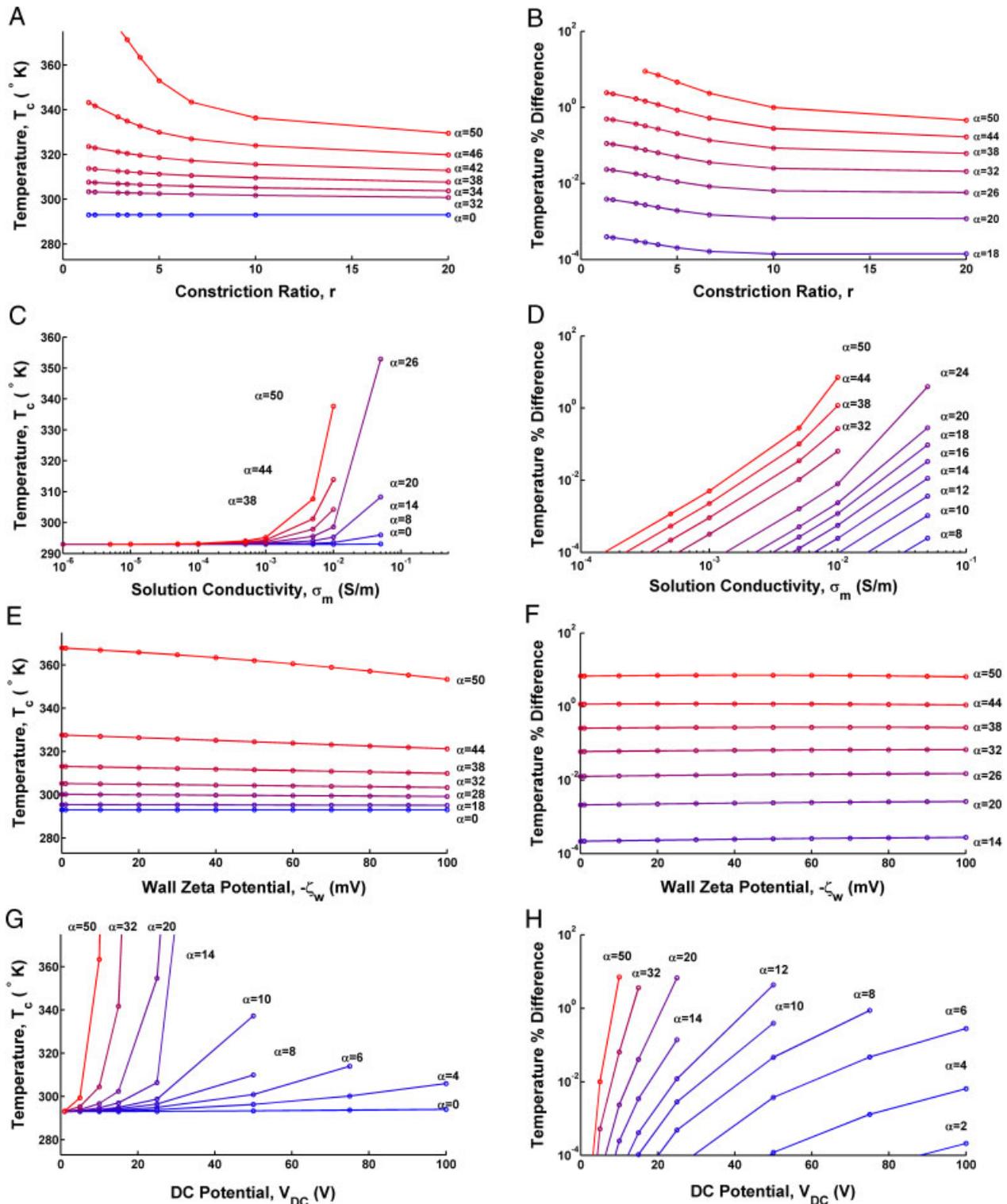
Figure 4. The mean constriction temperature (region defined in Fig. 1) is plotted for the datum state (Table 2, including the ET body force term) with variations in r, σ_m, ζ_w, and V_{DC} in the left-hand column (A, C, E, and G). The percentage difference in $\bar{T}_c$ between solutions with and without an ET body force term are plotted in the right-hand column (B, D, F, and H).

and thereby indirectly affects particle deflection. This can be seen in Figs. 5D and E, where particle deflection is independent of solution conductivity below 1×10^{-3} S/m. The

variations observed at high conductivities and high α are the result of increasing ET effects. ET effects increase significantly with increasing σ_m, especially where
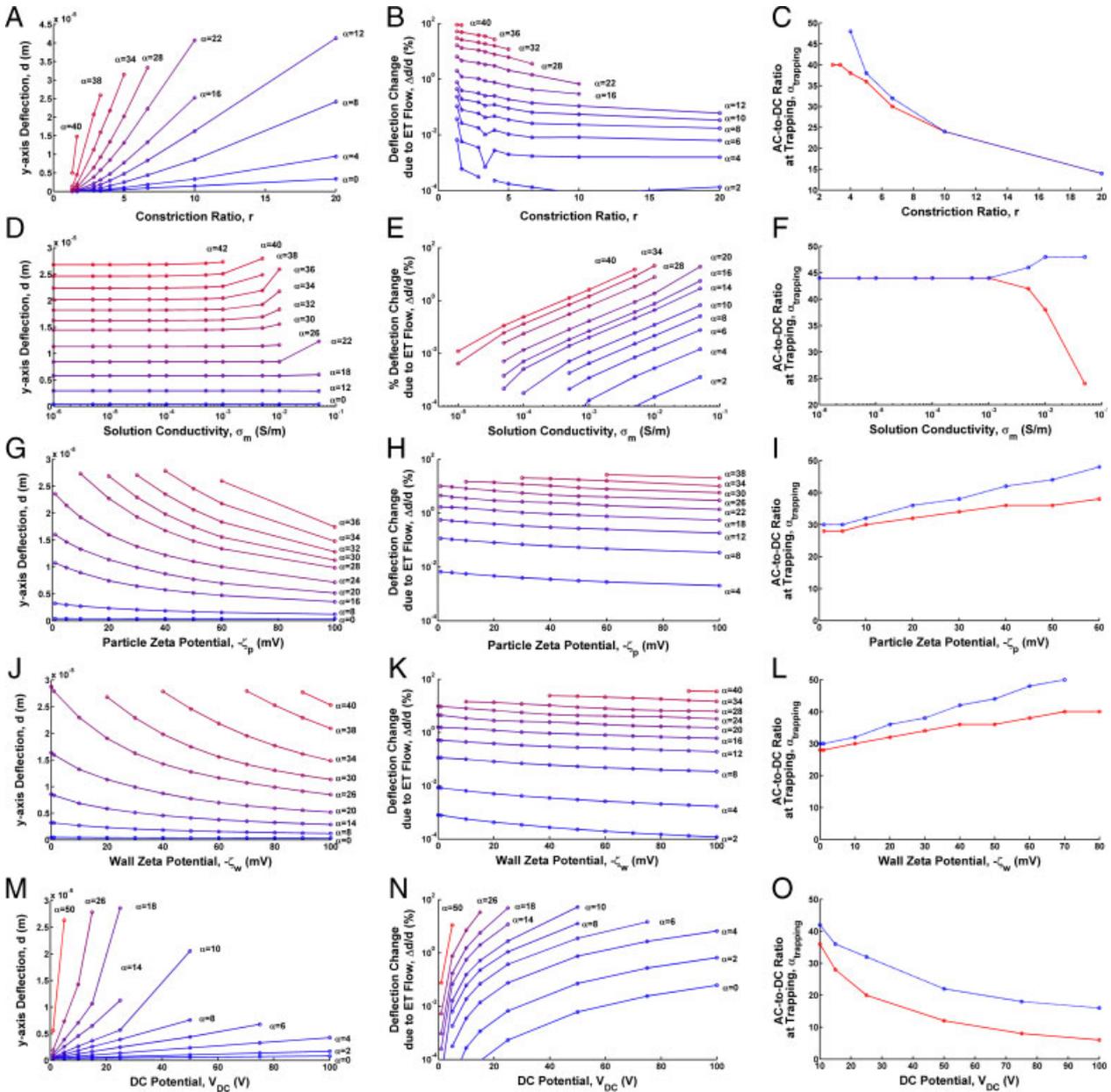
Figure 5. Particle trajectory analysis data for the datum state (Table 2) with variations in r (A, B, C), σ_m (D, E, F), ζ_p (G, H, I), ζ_w (J, K, L), and V_{DC} (M, N, O). Particle deflection with the ET body force is plotted in the left-hand column in (A, D, G, J, and M). Percentage difference in particle deflection between simulations with and without the ET body force term is plotted in the center column in (B, E, H, K, and N). Finally, $\alpha_{trapping}$ is plotted in the right-hand column in (C, F, I, L, and O). In left and center columns, line color (online) corresponds to α, varying from 0 (blue) to 50 (red) and increasing upward. In the right column, the line color (online) corresponds to data with (solid red, lower) and without (dashed blue, upper) ET flow.

$\sigma_m \geq 1 \times 10^{-3}$ S/m and $\alpha \geq 25$ (Fig. 5E). Based on deflection data shown in Fig. 5D, $\alpha_{trapping}$ is expected to be independent of σ_m at low conductivities and to decrease at higher conductivities. In these cases, at values of σ_m above $\sim 1 \times 10^{-3}$, ET flow decreases $\alpha_{trapping}$ (Fig. 5F).

Increasing the magnitude of the particle zeta potential, $|\zeta_p|$, decreases particle deflection and decreases the effects of electrothermal flow. Increasing the particle EP mobility *via* increases in $|\zeta_p|$ decreases the relative impact of iDEP

deflection (Fig. 5G). Similarly, the impact of variations in the fluid velocity field owing to the ET body force also decreases with increasing $|\zeta_p|$ (Fig. 5H). For the same reason particle deflection decreases with increasing $|\zeta_p|$, the value of the AC-to-DC ratio necessary to trap particles also increases: ET flow enhances particle trapping by decreasing the fluid velocity transporting particles toward the constriction (Fig. 5I). This effect, augmented slightly by increasing $|\zeta_p|$, shifts particle pathlines toward regions of slower fluid flow

and larger nDEP force (*i.e.* toward constriction corners as shown in Fig. 2).

Channel wall zeta potential, ζ_w, determines the EO mobility and the magnitude of the associated slip boundary condition. Increasing $|\zeta_w|$ increases the EO fluid velocity at the channel boundaries, decreasing particle deflection (Fig. 5J), diminishing the effects of ET flow (Fig. 5K), and increasing α_{trapping} (Fig. 5L). The increasing difference between α_{trapping} in simulations with and without ET flow is attributable to particle pathline distortion from increasing EO fluid flow, similar to the mechanism described above for particle electrophoresis (ζ_p).

Increasing the DC magnitude of the electric field has a number of effects. Particle electrophoresis and fluid electroosmosis both increase with increasing V_{DC}, as does Joule heating within the channel, leading to increased ET effects. α is scaled by V_{DC}, *i.e.* the AC field magnitude at $\alpha = 10$ increases as V_{DC} increases. As V_{DC} increases particle deflection increases (Fig. 5M). The electrothermal contribution to particle deflection also increases (Fig. 5N). The value of α_{trapping} decreases with increasing V_{DC} because the ohmic power input is approximately proportional to $(\alpha V_{\text{DC}})^2$ and the resulting electrothermal flow increases (Fig. 5O). While particle electrophoresis and electroosmosis increase $\propto \mathbf{E}$, Joule heating scales $\propto \mathbf{E}^2$, which likely accounts for the decrease in α_{trapping} from ET effects (Fig. 5O).

In this work, we examine particle trajectories as a result of EO, EP, and iDEP phenomena with coupled Joule heating and ET flow effects in polymeric iDEP devices using DC-offset, AC electric fields. We focus on the effects of channel constriction ratio, solution conductivity, and electrokinetic mobilities. Other researchers have studied iDEP particle deflection numerically and experimentally as a technique for size-based separation [37–39]. The role of channel geometry has been examined experimentally using an oil drop within the channel to change the constriction ratio [53, 55]. Additional work, utilizing DC-biased, AC electric fields, used an

insulating constriction to focus particles using iDEP [20]. Temperature effects were neglected in each of these cases, because the experiments could be run in a low-conductivity buffer. Figures 5D–F show that ET effects have the potential to alter the predicted particle trajectories when experiments are run with physiological media where conductivities are in the range of 1 S/m.

In contrast to the results presented here, where ET effects generated near an insulating constriction decreased the fluid velocity, other researchers have leveraged ET flows to enhance fluid flow and even pump fluids. Manoochehri *et al.* utilized asymmetric electrodes strategically placed on channel constrictions to enhance AC ET pumping [24, 34]. Electrode asymmetry creates counter-rotating vortices of different sizes, resulting in net bulk fluid flow. By placing one of the electrodes on top of a constriction and the other in a groove, the pumping velocity was increased because the counter-flow vortex was displaced away from the bulk fluid. ET effects have also been used to enhance mixing in microfluidic devices [35, 56].

The key conclusions drawn from our thermal simulations – that channel geometry influences the equilibrium channel temperature and that the temperature distribution within the channel is shifted by heat convection – are consistent with the previous studies of ET flow in microfluidic devices. Simulations of Joule heating in microfluidic devices have generally focused on electrode-based systems and static fluids [31, 57]. One notable exception is work done by Kates and Ren [58], who numerically studied a diverging microfluidic channel used for IEF. Their IEF experiments rely on a continuous pH gradient, set up by temperature gradients generated by the application of an electric field to a diverging channel. They performed 3D, numerical simulations of a diverging channel and the surrounding substrate with natural heat convection outside the device. Their work examined static and moving fluids and found that heat convection shifted the temperature distribution significantly. Additionally, they found that the channel geometry
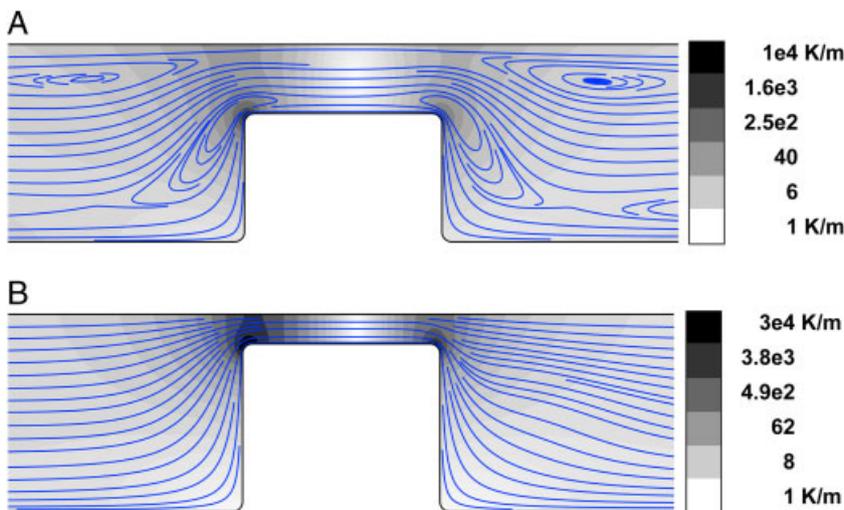

Figure 6. Fluid streamlines (blue, color online) at different constriction ratios show that recirculation is suppressed at higher constriction ratios, a result of higher EO flow boundary conditions within the constriction region. Simulation parameters are identical and listed in Table 2 with $\alpha = 40$ and $r = 2.86$ in (A) and $r = 6.67$ in (B). Filled contours correspond to temperature gradient magnitude and are logarithmic. The highest contour groups all temperature gradient magnitudes above 1×10^4 K/m: (A) Maximum 3.2×10^4 K/m); and 3×10^4 K/m: (B) Maximum 4.6×10^4 K/m) for clarity. Several streamlines are terminated for clarity.

(the angle of the diverging channel) significantly influenced the channel temperature.

Like the current work, the majority of numerical work examining ET flow near electrodes and particle deflection in iDEP devices is two dimensional. When extending this work to a three-dimensional domain, *i.e.* to ridged structures or constrictions in depth [19], we expect that the results to qualitatively describe fluid and particle behavior perpendicular to such constrictions, provided the constriction is long compared with the depth of the channel. Confounding factors, such as angled constrictions and curved constrictions, can potentially change the local electric and fluid velocity fields. However, if the electric field does not change significantly along the constriction, a two-dimensional approximation is justified perpendicular to the constriction, and the local ET body forces remain unchanged. Extensions to three-dimensional iDEP devices are not expected to alter the trends identified by this work.

4 Concluding remarks

This work has numerically investigated the effects of ET flow on the mean channel temperature and particle trajectories in a polymeric iDEP device at finite thermal Péclet number as a function of channel geometry (r), electric field parameters (α and V_{DC}), and particle and device properties (ζ_p and ζ_w). These simulations include coupled fluid, electrical, and thermal equations *via* temperature-dependent material properties such as solution conductivity and permittivity, thermal conductivity, specific heat, and viscosity.

The results show that heat convection contributes to the temperature distribution and temperature gradients responsible for ET flows. The average constriction temperature is a strong function of solution conductivity and electric field magnitude, with weak dependence on the constriction ratio. While convective heat transfer significantly alters the temperature distribution and determines the ET flow field, it can usually be neglected when calculating the mean constriction temperature. $\bar{T}_c$ changes less than 1% due to ET effects except as $\alpha \rightarrow 50$, in which case the error can approach ∼10%. Particle deflection is a strong function of constriction ratio, as ET effects increase particle deflection more than 10% when the constriction ratio is ≤ 8 and $\alpha \geq 38$. Solution conductivity plays an important role in determining the temperature in the channel and the magnitude of ET effects. As $\sigma_m \geq 1 \times 10^{-2}$ and $\alpha \rightarrow 40$, ET effects make more than a 10% difference in particle deflection. Increasing particle and wall zeta potentials ($|\zeta_p|$, $|\zeta_w|$) decrease particle deflection, but act independent of ET effects, with no appreciable change in ET contributions to particle deflection over the range of ζ_p and ζ_w tested in this work. Varying the DC field magnitude significantly alters particle trajectories and also increases ET effects. The net result of increasing V_{DC} is to increase particle deflection and increase the ET augmentation of deflection. These quantitative results are applicable for a Zeonor microfluidic iDEP device under the datum conditions listed in Table 2.

While the quantitative results are specific only to the geometry under study, the trends are clear: $\bar{T}_c$ is a strong function of σ_m and V_{DC}; particle deflection and trapping are strong functions of r and V_{DC}, relatively weak functions of ζ_p and ζ_w, and nearly independent of σ_m; and ET effects are significant at high electric fields and in solutions of high conductivity. These results are qualitatively consistent with our previous experimental and simulation work [19] and anecdotal explanations for recirculating particle motion in other iDEP devices. Changes in effective solution conductivity can also be induced by particle concentration variations [59, 60] rather than local temperature variations. In this work, we assume non-interacting particles at a low volume fraction. The results for particle deflection are unlikely to be affected by particle concentration variations because deflection causes minimal concentration changes. In the case of particle trapping, however, particle volume fraction will increase over time, increasing the effective solution conductivity and further enhancing the effects of fluid forces caused by conductivity inhomogeniety. This accumulation of particles however, only occurs as $\alpha \rightarrow \alpha_{\mathrm{trapping}}$, and so we expect that the results presented here will be applicable across a reasonable range of particle concentrations. In all the cases examined in this work, ET forces (regardless of the source of conductivity variation) point away from the constriction, decreasing the EO fluid velocity upstream of the constriction and thereby *enhancing* particle deflection and trapping. This work supported by the NSF via grant CBET-0828997 and a graduate research fellowship to Benjamin G. Hawkins.

The authors have declared no conflict of interest.

5 References

[1] Pohl, H. A., *Dielectrophoresis: The Behavior of Neutral Matter in Nonuniform Electric Fields*, Cambridge University Press, Cambridge 1978.

[2] Jones, T. B., *Electromechanics of Particles*, Cambridge University Press, New York 1995.

[3] Kirby, B. J., *Micro- and Nanoscale Fluid Mechanics: Transport in Microfluidic Devices*, Cambridge University Press, Cambridge 2010.

[4] Hawkins, B. G., Gleghorn, J. P., Kirby, B. J., *Dielectrophoresis for Particle and Cell Manipulations*, Artech House, Boston, Chapter 6, 2009, pp. 133–182.

[5] Sanchis, A., Brown, A. P., Sancho, M., Martnez, G., Sebastián, J. L., Muñoz, S., Miranda, J. M., *Bioelectromagnetics* 2007, *28*, 393–401.

[6] Lapizco-Encinas, B. H., Simmons, B. a., Cummings, E. B., Fintschenko, Y., *Anal. Chem.* 2004, *76*, 1571–1579.

[7] Cho, Y.-K., Kim, S., Lee, K., Park, C., Lee, J.-G., Ko, C., *Electrophoresis* 2009, *30*, 3153–3159.

[8] Errachid, A., Castellarnau, M., Madrid, C., Juárez, A., Samitier, J., *Biophys. J.* 2006, *91*, 3937–3945.

[9] Yang, J., Huang, Y., Wang, X.-B., Becker, F. F., Gascoyne, P. R. C., *Anal. Chem.* 1999, *71*, 911–918.

[10] Yang, J., *Biophys J.* 2000, *78*, 2680–2689.

[11] Gascoyne, P., Noshari, J., Becker, F., Pethig, R., *IEEE Trans. Ind. Appl.* 1994, *30*, 829–834.

[12] Das, C. M., Becker, F., Vernon, S., Noshari, J., Joyce, C., Gascoyne, P. R. C., *Anal. Chem.* 2005, *77*, 2708–2719.

[13] Chou, C. F., Tegenfeldt, J. O., Bakajin, O., Chan, S. S., Cox, E. C., Darnton, N., Duke, T., Austin, R. H., *Biophys. J.* 2002, *83*, 2170–2179.

[14] Clarke, R. W., White, S. S., Zhou, D., Ying, L., Klenerman, D., *Angew. Chem. Int. Ed. Engl.* 2005, *44*, 3747–3750.

[15] Clarke, R., Piper, J., Ying, L., Klenerman, D., *Phys. Rev. Lett.* 2007, *98*, 198102–198106.

[16] Hölzel, R., Calander, N., Chiragwandi, Z., Willander, M., Bier, F., *Phys. Rev. Lett.* 2005, *95*, 128102–128104.

[17] Lapizco-Encinas, B. H., Ozuna-Chacón, S., Rito-Palomares, M., *J. Chromatogr. A* 2008, *1206*, 45–51.

[18] Hughes, M., Morgan, H., Rixon, F., Burt, J., Pethig, R., *Biochim. Biophys. Acta* 1998, *1425*, 119–126.

[19] Hawkins, B. G., Smith, A. E., Syed, Y. A., Kirby, B. J., *Anal. Chem.* 2007, *79*, 7291–7300.

[20] Zhu, J., Xuan, X., *Electrophoresis* 2009, *30*, 2668–2675.

[21] Xuan, X., *Electrophoresis* 2008, *29*, 33–43.

[22] Mueller, T., Gerardino, A., Schnelle, T., Shirley, S. G., Bordoni, F., De Gasperis, G., Leoni, R., Fuhr, G., *J. Phys. D Appl. Phys.* 1996, *29*, 340–349.

[23] Park, S., Koklu, M., Beskok, A., *Anal. Chem.* 2009.

[24] Du, E., Manoochehri, S., *J. Appl. Phys.* 2008, *104*, 064902.

[25] Fuhr, G., Hagedorn, R., Muller, T., Benecke, W., Wagner, B., *J. Microelectromech. Syst.* 1992, *1*, 141–146.

[26] Oh, J., Hart, R., Capurro, J., Noh, H. M., *Lab Chip* 2009, *9*, 62–78.

[27] Morgan, H., Hughes, M. P., Green, N. G., *Biophys. J.* 1999, *77*, 516–525.

[28] Jang, L.-S., Huang, P.-H., Lan, K.-C., *Biosens. Bioelectron.* 2009, *24*, 3637–3644.

[29] Gagnon, Z., Chang, H.-C., *Electrophoresis* 2005, *26*, 3725–3737.

[30] Cao, J., Cheng, P., Hong, F., *J. Electrostat.* 2008, *66*, 620–626.

[31] Williams, S. J., Chamarthy, P., Wereley, S. T., *J. Fluid. Eng.* 2010, *132*, 021103.

[32] Perch-Nielsen, I. R., Green, N. G., Wolff, A., *J. Phys. D Appl. Phys.* 2004, *37*, 2323–2330.

[33] Lian, M., Wu, J., *Microfluid. Nanofluidics* 2009, *7*, 757–765.

[34] Du, E., Manoochehri, S., *Electrophoresis* 2008, *29*, 5017–5025.

[35] Cao, J., Cheng, P., Hong, F. J., *Microfluid. Nanofluidics* 2007, *5*, 13–21.

[36] Barrett, L. M., Skulan, A. J., Singh, A. K., Cummings, E. B., Fiechtner, G. J., *Anal. Chem.* 2005, *77*, 6798–6804.

[37] Hyoung Kang, K., Xuan, X., Kang, Y., Li, D., *J. Appl. Phys.* 2006, *99*, 064702.

[38] Kang, K. H., Kang, Y., Xuan, X., Li, D., *Electrophoresis* 2006, *27*, 694–702.

[39] Kang, Y., Li, D., Kalams, S. A., Eid, J. E., *Biomed. Microdevices* 2008, *10*, 243–249.

[40] Kang, Y., Cetin, B., Wu, Z., Li, D., *Electrochim. Acta* 2009, *54*, 1715–1720.

[41] Srivastava, S. K., Daggolu, P. R., Burgess, S. C., Minerick, A. R., *Electrophoresis* 2008, *29*, 5033–5046.

[42] Jackson, J. D., *Classical Electrodynamics*, Wiley, New York, 3rd Edn., 1998.

[43] Ramos, A., Morgan, H., Castellanos, A., *J. Phys. D Appl. Phys.* 1998, *31*, 2338–2353.

[44] White, F. M., *Viscous Fluid Flow*, McGraw-Hill, New York, 3rd Edn., 2003.

[45] Lyklema, J., *Fundamentals of Interface and Colloid Science: Volume II: Solid–Liquid Interfaces*, Academic Press, New York, NY 1995.

[46] Tandon, V., Bhagavatula, S. K., Nelson, W. C., Kirby, B. J., *Electrophoresis* 2008, *29*, 1092–1101.

[47] Tandon, V., Kirby, B. J., *Electrophoresis* 2008, *29*, 1102–1114.

[48] Castellanos, a., Ramos, a., González, a., Green, N. G., Morgan, H., *J. Phys. D Appl. Phys.* 2003, *36*, 2584–2597.

[49] CRC. *CRC Handbook of Chemistry and Physics*, Knovel, Binghamton, NY, 90 Edn., 2010.

[50] Bejan, A., *Heat Transfer*, Wiley, New York, NY 1993.

[51] Zeon Chemicals, Zeonor 1020R Datasheet, 2009.

[52] Loire, S., Mezic, I., *42nd IEEE International Conference on Decision and Control* 2003, *6*, 6448–6453.

[53] Barbulovic-Nad, I., Xuan, X., Lee, J. S. H., Li, D., *Lab Chip* 2006, *6*, 274–279.

[54] Zhu, J., Tzeng, T.-R. J., Xuan, X., *Electrophoresis* 2010, *31*, 1382–1388.

[55] Thwar, P. K., Linderman, J. J., Burns, M. A., *Electrophoresis* 2007, *28*, 4572–4581.

[56] Feldman, H. C., Sigurdson, M., Meinhart, C. D., *Lab Chip* 2007, *7*, 1553–1559.

[57] Xuan, X., *Electrophoresis* 2008, *29*, 33–43.

[58] Kates, B., Ren, C. L., *Electrophoresis* 2006, *27*, 1967–1976.

[59] Trau, M., Sankaran, S., Saville, D. A., Aksay, I. A., *Nature* 1995, *374*, 437–439.

[60] Trau, M., Sankaran, S., Saville, D. A., Aksay, I. A., *Langmuir* 1995, *11*, 4665–4672.